Direct Observation of Halide Migration and its Effect on Photoluminescence of Methylammonium Lead Bromide Perovskite Single Crystals

*Yanqi Luo,[1] Parisa Khoram,[2] Sarah Brittman,[2] Zhuoying Zhu,[1] Barry Lai[3], Shyue Ping Ong,[1] Erik C. Garnett,[2] David P. Fenning [1, *]*

[1] Department of Nanoengineering, University of California San Diego, La Jolla, CA 92093. *dfenning@eng.ucsd.edu
[2] Center for Nanophotonics, FOM Institute AMOLF, Amsterdam, the Netherlands
[3] Advanced Photon Source, Argonne National Laboratory, Argonne, IL 60439

Keywords: Hybrid perovskite, halide migration, nanoprobe x-ray fluorescence, spatially-resolved photoluminescence mapping, nudged elastic band (NEB) and DFT computation

Optoelectronic devices based on hybrid perovskites have demonstrated outstanding performance within a few years of intense study. However, commercialization of these devices requires overcoming barriers to their development, such as chemical instability under operating conditions. To investigate this instability and its consequences, we varied the electric field applied to single crystals of methylammonium lead bromide ($CH_3NH_3PbBr_3$) and mapped changes in both their elemental composition and photoluminescence. Synchrotron-based nanoprobe X-ray fluorescence (nano-XRF) with 250 nm resolution revealed quasi-reversible field-assisted halide migration, with corresponding changes in photoluminescence. We observed that higher local bromide concentration was correlated to superior optoelectronic performance in $CH_3NH_3PbBr_3$. A lower limit on the electromigration rate is calculated from these experiments, and we interpret the motion as vacancy-mediated migration based on nudged elastic band density functional theory simulations. The XRF mapping data provides direct evidence of field-assisted ionic migration in a model hybrid perovskite thin single crystal, while the link with photoluminescence proves the halide stoichiometry plays a key role in the optoelectronic properties of the perovskite.

Halide perovskite materials have shown promise for a wide range optoelectronic applications including light-emitting diodes,[1] photonic lasers,[2] and solar cells[3,4] Despite their impressive potential demonstrated in laboratory devices, questions remain regarding many of the fundamental properties that govern their performance limits, especially their stability under hot,[5] humid,[6] illuminated[7] and biased operating conditions.[8] Understanding both the origin of this instability and its connection to performance is key to developing perovskite optoelectronic devices beyond the laboratory. In particular, the hysteresis of scanning current-voltage measurement is detrimental in evaluating and comparing the optoelectronic performance of perovskite precisely and may indicate the presence of performance-limiting defects.

Many groups have suspected ionic migration under an electric field and illumination as an important limiting mechanism in hybrid perovskite devices, particularly in regard to current-voltage sweep hysteresis.[9–13] Assuming thermal equilibrium and non-interacting defects, perovskites are predicted to have a high concentration of vacancies (10^{17}-10^{20} cm^{-3} for $CH_3NH_3PbI_3$).[14] Evidence of vacancy-mediated diffusion of X-site anions (in the ABX_3 structure) with low activation energy through the conventional hopping mechanism along the anion octahedral edge has been determined for oxide[15] and inorganic halide perovskites.[16] In the analogous hybrid halide perovskites, extensive computational investigations, particularly in the methylammonium lead iodide ($CH_3NH_3PbI_3$) system, have shown that I^- is likely the most mobile ion because it exhibits a lower energy barrier to migration in comparison to Pb^{2+} and $CH_3NH_3^+$.[9,12,17] Several groups have observed ionic migration of both organic cations and halide anions and in $CH_3NH_3PbI_3$ and $CH_3NH_3PbI_{3-x}Cl_x$ using energy-dispersive X-ray spectroscopy (EDS),[10,18] time-of-flight secondary-ion-mass spectrometry (tof-SIMS),[19] X-ray photoemission spectroscopy (XPS)[20] and IR microscopy mapping techniques.[18] These analytical techniques each have their own specific limitations. For instance, tof-SIMS involves sample fragmentation and physical destruction of the investigated area; [21] IR microscopy can

detect bond stretches of the organic components in perovskite films but is generally not sensitive to the low-frequency vibrations of the inorganic components;[22] and XPS is sensitive only to the first few nanometers near the surface and requires high vacuum condtions. EDS must be applied with caution to halide perovskites because of their sensitivity to electron beam damage.[7,23] Finally, the nano-XRF technique maps heavy elements throughout the bulk of the sample with higher spatial resolution and sensitivity than XPS, tof-SIMS, EDX or IR microscopy.

Recently, synchrotron-based scanning nanoprobe X-ray fluorescence (nano-XRF) has been shown to be an effective probe of local composition in hybrid perovskite devices without affecting the elemental distribution.[24–26] During nano-XRF measurement, a focused X-ray beam excites core-shell electrons from the atoms in the sample. When a core-hole is filled by relaxation of an outer shell electron, a fluorescent photon is emitted, and its energy identifies the element from which it came due to the characteristic energy of electronic transitions. As a photon-in, photon-out process, nano-XRF is dose-efficient – critical for radiation-sensitive materials like the hybrid perovskites – and enables nanoscale elemental mapping with part per million sensitivity for elements heavier than sodium.[27] The many-millimeter working distance at hard X-ray energies also facilitates *in situ* and *in operando* studies.[25]

The best way to provide a direct link between composition and performance is to combine spatially-resolved elemental or chemical detection methods with techniques that probe the material's local optoelectronic properties. Luminescence spectroscopy and imaging are versatile techniques to probe recombination mechanisms and dynamics in semiconductors. For example, recently researchers have used spatially-resolved luminescence to reveal the role of Cl in $CH_3NH_3PbI_{3-x}Cl_x$,[28] to correlate contact resistance with morphology,[29,30] and to understand the degradation of the perovskite layer[31] and its interfaces.[30] Despite the importance of ionic migration, open questions remain as to how stoichiometric changes affect photoluminescence – a property directly linked to device performance.[32,33]

In this study, we identify a direct relationship between halide migration and local optoelectronic quality. Direct elemental evidence of halide migration in a $CH_3NH_3PbBr_3$ single crystal is detected using nano-XRF. Thin single crystals[34] of $CH_3NH_3PbBr_3$, which are tens of microns wide and ~500 nm thick, are used as a model system to study the fundamental properties of ionic migration in hybrid perovskites, avoiding complications from grain boundaries that are present in perovskite thin films. In response to an applied electric field, local stoichiometric variations appear along the crystal, which are correlated to local changes in the PL intensity. PL intensity increases in halide-rich regions and decreases in halide-poor ones, with quasi-reversible variation observed over multiple voltage biasing cycles. Furthermore, nudged elastic band (NEB) density functional theory (DFT) computations confirm that Br^- ions experience a low energy barrier to migration within the $CH_3NH_3PbBr_3$ structure. The direct link between local stoichiometry and optoelectronic quality also clarifies that halide migration is a challenge that is intrinsic to the absorber and one that may play a determining role in the ultimate performance limits of perovskite devices.

Nano-XRF mapping is used to identify the spatial distribution of elements within a $CH_3NH_3PbBr_3$ single crystal under applied bias. The crystals span Pt electrodes, and the voltage is applied laterally across the device as shown in **Figure 1**. Pt electrodes prevent any driving force from a difference in the work functions of two different metals and also minimize chemical reactions or diffusion[35] of metallic atoms at the metal/perovskite interface.[36] Prior to the XRF measurement, electrical contact between the perovskite crystal and Pt electrodes was confirmed by current-voltage (I-V) scans (**Figure S1)**. Fluorescence spectra were collected at each point during the XRF mapping using a synchrotron X-ray beam with a 250 nm full-width half maximum. **Figure 2a** shows the corresponding optical micrograph of the $CH_3NH_3PbBr_3$ crystal studied by XRF. As expected, the spatial distribution and elemental composition of the crystals are uniform on the 250-nm length scale of measurement during repeated X-ray mapping without bias under the focused 13.6 keV X-ray beam with a flux of

2.37×10^9 photons/sec (**Figure S2)**. Note that the light elements in the methylammonium cation are not detectable by XRF, but the major heavy elements Pb and Br are detectable with sensitivity down to parts per million.

The local Br:Pb stoichiometry within the $CH_3NH_3PbBr_3$ single crystal is initially homogeneous across the crystal but changes systematically during application of an external electric field (**Figure 2b)**. The seven XRF maps of the Br:Pb atomic ratio in the 30 x 30 μm^2 crystal are arranged from left (Map 1) to right (Map 7) based on the chronological sequence of applied bias. Map 1 is the initial scan showing the Br:Pb atomic ratio. As expected, the initial area-averaged Br:Pb ratio across the crystal was 3.08 +/- 0.2. An arrow above each XRF map measured under bias indicates the direction of the electric field, where the left electrode is held at ground and the right electrode has the applied voltage bias V_{app} (orange arrow: V_{app} = -2V and blue arrow: V_{app} = +2V). The Br:Pb ratio is plotted because it removes the effects of small spatial variations in thickness, but the shift in Br:Pb ratio seen in **Figure 2b** results entirely from a change in the Br distribution, as the Pb distribution remains constant throughout the XRF mapping (**Figure S3**).

To examine the migration in detail, the perovskite crystal underwent a total of three poling cycles, from unbiased to +/- 2V bias to unbiased. After collecting the initial unbiased map (left of **Figure 2b**), a -2V DC bias was applied. After 30 minutes of bias applied without X-ray irradiation, we collected an XRF map (~25 min duration) with the bias still applied to observe the effect of the electric field. The change in the Br:Pb atomic ratio between Maps 1 and 2 clearly indicates depletion of Br above the electrode at lower potential (right Pt pad). This depletion is consistent with the direction that Br^- anions would migrate. The bias was then removed, and after a 30 min relaxation period, a third XRF map was taken to visualize any diffusion along the Br concentration gradient. The Br concentration is then slightly depleted over the left-hand electrode as Br- diffuses back in the absence of bias.

When the direction of the bias is reversed (+2V), the Br shifts toward the positively biased electrode, also consistent with migration of Br^- anions. A significant Br shift away from the left-hand negative electrode is observed in Map 4, while the Br concentration recovers slightly on the right-hand electrode (Map 2 vs 4). Upon subsequent relaxation in Map 5, a small recovery in the Br distribution is again seen. The last cycle seen in Maps 6 and 7 repeats the same -2V and 0V bias condition as Maps 1 and 2, respectively, and confirms that the observed changes in the Br:Pb distribution are repeatable. Given the observed migration across the 10 μm electrode gap within 30 min at a 2V bias, the lower bound estimate of Br mobility at room temperature is $2.78\times10^{-10}\mathrm{cm}^2/(\mathrm{V}\cdot\mathrm{s})$ (see SI for details).

To assess the migration of Br^- within the crystal more quantitatively, the changes in average Br:Pb atomic ratio above each of the two electrodes are presented in **Figure 2c**. The average ratio is plotted with respect to time and applied bias. As Br:Pb increases on one electrode, a decreasing ratio is seen on the other, providing additional support for an ion migration mechanism. The largest Br concentration change occurs above the lower potential electrode (Electrode B) right after the first bias is applied, when the Br:Pb ratio drops from 3.0 ± 0.03 to 2.6 ± 0.07. All subsequent changes are smaller, and the Electrode B area never recovers fully its initial Br concentration. On the other hand, Electrode A exhibits a more reversible response to applied bias and largely recovers from the smallest Br:Pb ratio near 2.8 ± 0.09 to 2.9 ± 0.06 after final relaxation. A secondary analysis of the Br variation under applied bias is conducted using the center of mass of the Br:Pb distribution to reveal the bias-dependent direction of Br migration (**Figure S4)**. The shifts of center of mass of the Br:Pb distribution across the entire crystal are consistent with the Br concentration changes above the electrodes in Figure 2. Small, severely Br-deficient regions evidenced by localized dark spots in **Figure 2b** develop above both electrodes over time. These regions indicating indicate local degradation of the perovskite phase and possible formation of $PbBr_2$. After biasing the crystal for 4 hours, the area-averaged Br:Pb ratio in the last XRF map (rightmost) is 2.69. The loss of Br occurs

predominantly during the first negative bias of each electrode, after which the total average concentration of Br was fairly stable (**Figure S5)**. Given what appears to be nanoscopic local formation of $PbBr_2$ in some regions, one could speculate that trace amounts of MABr leaves the sample in an electrochemical reaction in regions of negative bias under X-ray irradiation. On the other hand, little change of the Br:Pb ratio away from 3.0 is observed between the electrode gap throughout the biasing cycles. Overall, the Br:Pb distribution shifts in the direction opposite the applied field at all time points.

A fresh $CH_3NH_3PbBr_3$ microcrystal, (optical image shown in **Figure 3a**, I-V scan in **Figure S1**), from the same sample chip is used to explore how the local optoelectronic properties vary in response to a similar bias sequence used in the nano-XRF experiments**.** The crystal was excited using a 15 μW, 405-nm continuous-wave violet laser while performing PL mapping before, during, and after bias. (Each map is shown in **Figure S6** and took ~30 min to be collected.) PL spectra were collected for each point of the crystal by moving the stage in the X and Y directions by 333 nm steps. PL maps were constructed from the integration of the total emission intensity over the wavelength 500-580 nm. Enhancement of PL intensity under bias at the forward biased electrode and its reduction at the reverse biased electrode is attributed to the change of the depletion region width at each contact. Similar changes in PL emission intensity with the variation of dc bias were reported in other semiconductors such as InP, GaAs and chalcopyrite ($CuGaSe_2$).[37–39]. To compare crystals at the same bias condition, the PL emission spectra averaged over the area of each electrode (area A and B) were collected at zero bias after applying and removing the electric field as shown in **Figure 3b-c**. An increase in PL intensity relative to its initial value was observed in the region above the electrode previously held at higher potential. A decrease was observed over the contact at lower potential. According to the XRF maps in Figure 2, the contact with the higher potential is where the Br concentration is higher; therefore, the Br^- rich regions exhibit enhanced PL after removal of the electric field.

Figures 3d-e show the spatial variation of PL intensity across the crystal in response to biasing as the percentage change of PL intensity (ΔPL%). Each map represents the percentage change of PL after removing the electric field and returning the crystal to the initial 0V condition. (Details of the calculation are in the supporting information.) The orange and blue arrows on figures 3d and 3e, respectively, show the electric field that the crystal experienced before collecting the PL maps. Comparing the relative changes with the direction of the electric field, one sees that the PL intensity increases in the region that experienced higher potential (see the red regions at left side Figure 3d and right side Figure 3e), and decreases in the region that was previously at lower potential (see the blue regions at right side figure 3d and left side figure 3e). This anti-correlation between Electrodes A and B after bias mirrors the trend seen in XRF. The bias-dependence of the local photoluminescence is confirmed in $CH_3NH_3PbBr_3$ crystals deposited onto different electrodes (Au-Au and Au-Ti electrodes) as shown in **Figure S7**, indicating that the increase of PL in the opposite direction of electric field is independent of the particular metal/perovskite interface. In all cases, the peak of the PL spectrum does not shift in energy significantly (less than 2 nm) between the Br-rich and Br-poor regions (see **figure S8**).

The PL mapping experiment was also done on the crystal that was exposed to the X-ray beam during XRF mapping, and its the PL spectra were comparable to those of a fresh crystal (figure S8 k and l) with the PL peak being blue shifted by 10 nm. A similar trend in PL intensity shift with electrical biasing is seen for this crystal, although the change in PL intensity is not as clear as it is for the fresh crystals (Figure S9 b and c). Synchrotron X-ray irradiation has been shown to degrade carrier collection in hybrid perovskites within seconds of exposure at a single spot,[25] and it is thus not surprising that the PL changes are more clear in the fresh crystal.

The changes in PL intensity may be explained by vacancy-mediated halide migration. Initially, the PL intensity was inhomogeneous across the single crystal as seen in **Figure S6** suggesting that surface or bulk defects dominate the PL response. Upon applying bias across

the crystal, it is observed that Br moves opposite to the direction of the electric field and the local PL increases where Br increases. This enhanced PL in bromide-rich regions may originate from three distinct but related mechanisms, triggered by the ionic migration seen in the XRF maps (schematic of mechanisms in **Figure S10)**. First, bromide migration will lead to local changes in the bromide vacancy concentration, which has been proposed to play an important role in the photoluminescence quantum yield.[40–42]. Crystal point defects such as vacancies may act as non-radiative recombination centers; therefore, a higher Br vacancy concentration could lead to lower radiative recombination efficiency, causing the band-to-band PL intensity to decrease. Second, bromine stoichiometry may play a role in the density of interface states at the contacts. The migration of the bromine away from the contact interface at the lower potential electrode may lead to a higher density of interface states, and at the other contact, the higher Br content may passivate interface states. Finally, ionic migration will cause some residual change in the potential at the perovskite/metal contact interface even after the electric field is removed, due to slow ionic diffusion. At the lower-potential contact the perovskite/metal interface behaves as in reverse bias: the residual change in potential increases the depletion region, which helps to split the photogenerated carriers and prevents them from recombining radiatively, suppressing PL intensity. At the higher-potential contact the interface behaves as in forward bias: the depletion region becomes smaller and PL intensity is enhanced. Further studies are necessary to quantify the relative importance of each mechanism. Self-trapped carriers in the crystal lattice (strong-coupled polarons) have been suggested to play a role in charge carrier dynamics of hybrid perovskites and affect radiative recombination rate.[43] In the case of polaron formation, a red shift in the energy of the PL peak is expected, but no red shift was resolved within the detection limit of the PL setup in this study (SI, figure S8). Continued detailed study of ionic migration is critical because vacancies, as inherent material defects, may act as mediator or direct participants in non-radiative recombination centers in $CH_3NH_3PbBr_3$.

The experimentally observed changes in Br concentration in the $CH_3NH_3PbBr_3$ single crystal are substantiated by the low energetic barrier to migration of Br- found by DFT climbing-image nudged elastic band (CI-NEB) calculations. To elucidate the ionic migration mechanism under applied bias, CI-NEB calculations were performed using 2x2x2 supercells (computational details in SI). CI-NEB is a common method for finding minimum energy paths for ion migration.[44–46] A single positively-charged Br^- vacancy (V_{Br}^+) was introduced, and overall charge neutrality was achieved via a compensating background charge. We find that the lowest energy configuration for pristine $CH_3NH_3PbBr_3$ is in which the polar methylammonium (MA) cations are aligned, which is the expected orientation under an applied bias.[12,18] This alignment of the MA cations breaks the cubic symmetry, resulting in three distinct migration paths for Br^-, which are shown in **Figure 4**. The energy-migration coordinate diagram and the corresponding pathways viewed in a supercell are presented in **Figure S11**. The hops where the Br^- moves with a component in the direction of the C-N bond alignment, denoted as BCB and BAB, show the lowest migration energy barriers of 227 meV and 306 meV, respectively. The other hop, CAC, shows a migration energy of 425 meV. The alignment of the MA cations under bias appears to create a channel with a lower energy of Br- vacancy migration along the field direction. In the absence of an electric field, this lowered barrier will be averaged out as methylammonium molecules are randomly oriented at room temperature per $MAPbBr_3$ single crystal neutron diffractometry.[47] Halide migration appears to benefit from MA alignment that results in a lower migration energy barrier under an applied bias. The migration, in turn, is correlated with the density of recombination active defects as evidenced by the changes seen in the photoluminescence response under bias.

In summary, we systematically manipulate the halide concentration laterally within a thin $CH_3NH_3PbBr_3$ single crystal by applying a voltage bias. We observe the changes of Br distribution at the nanoscale by means of Nano-XRF. The halide migration is directly correlated to variations in PL response. As Br^- migrates away from the negatively-biased electrode and

the perovskite becomes locally sub-stoichiometric, the PL intensity decreases. NEB calculations indicate that the alignment of the methylammonium cation under bias forms channels that facilitate halide migration along the field direction. Combining the quantitative analysis of ion migration with local optoelectronic characterization provides insight into the fundamental operation of halide perovskite devices. The link between intrinsic point defect migration and photoluminescence intensity makes it clear that controlling the crystal chemistry is paramount. Possible strategies to mitigate the effects of Br migration and improve optoelectronic performance in the perovskite include growing perovskites in halide-rich conditions[48] or applying post-growth treatments to lower the concentration of halide vacancies. Future work is needed to understand the defect kinetics of ion migration as a function of the absorber chemistry and to reveal the nature of the optoelectronic defects that arise under bias to achieve the full potential of the hybrid perovskite materials for optoelectronic devices.

Methods

Experimental and computational details can be found in supporting information.

Supporting Information

Supporting Information is available from the Wiley Online Library or from the author.

Acknowledgements

Y.L and P.K contributed to the work equally. The authors thank Dr. Esther Alarcón Lladó for helpful comments on the manuscript and Dirk-Jan Spaanderman for assistance in the schematic figure. Y.L. acknowledges the support of the UC Carbon Neutrality Initiative. DPF acknowledges UC San Diego start up funds and the support of the Hellman Foundation. This work is part of the research program in The Netherlands Organization for Scientific Research (NWO). PK and ECG acknowledge financial support from the European Research Council under the European Union's Seventh Framework Programme (FP/2007-2013)/ERC Grant Agreement No. 337328, "NanoEnabledPV". SFB acknowledges the grant from an industrial partnership between Philips and FOM. ZYZ and SPO acknowledge funding support from the U.S. Department of Energy, Office of Science, Basic Energy Sciences under Award No. DE-SC0012118 for the computational portion of the work, as well as computing resources provided by Triton Shared Computing Cluster (TSCC) at the UC, San Diego, the National Energy Research Scientific Computing Center (NERSC), and the Extreme Science and Engineering Discovery Environment (XSEDE) supported by National Science Foundation under Grant No. ACI-1053575. This research used resources of the Advanced Photon Source, a U.S. Department

of Energy (DOE) Office of Science User Facility operated for the DOE Office of Science by Argonne National Laboratory under Contract No. DE-AC02-06CH11357.

Reference.

[1] Z.-K. Tan, R. S. Moghaddam, M. L. Lai, P. Docampo, R. Higler, F. Deschler, M. Price, A. Sadhanala, L. M. Pazos, D. Credgington, F. Hanusch, T. Bein, H. J. Snaith, R. H. Friend, *Nat. Nanotechnol.* **2014**, *9*, 1.

[2] H. Zhu, Y. Fu, F. Meng, X. Wu, Z. Gong, Q. Ding, M. V Gustafsson, M. T. Trinh, S. Jin, X.-Y. Zhu, *Nat. Mater.* **2015**, *14*, 636.

[3] D. W. de Quilettes, S. M. Vorpahl, S. D. Stranks, H. Nagaoka, G. E. Eperon, M. E. Ziffer, H. J. Snaith, D. S. Ginger, *Sci.* **2015**, *348*, 683.

[4] K. Wojciechowski, S. D. Stranks, A. Abate, G. Sadoughi, A. Sadhanala, N. Kopidakis, G. Rumbles, C. Z. Li, R. H. Friend, A. K. Y. Jen, H. J. Snaith, *ACS Nano* **2014**, *8*, 12701.

[5] B. Conings, J. Drijkoningen, N. Gauquelin, A. Babayigit, J. D'Haen, L. D'Olieslaeger, A. Ethirajan, J. Verbeeck, J. Manca, E. Mosconi, F. De Angelis, H. G. Boyen, *Adv. Energy Mater.* **2015**, *5*, 1.

[6] G. E. Eperon, S. N. Habisreutinger, T. Leijtens, B. J. Bruijnaers, J. J. Van Franeker, D. W. Dequilettes, S. Pathak, R. J. Sutton, G. Grancini, D. S. Ginger, R. A. J. Janssen, A. Petrozza, H. J. Snaith, *ACS Nano* **2015**, *9*, 9380.

[7] E. T. Hoke, D. J. Slotcavage, E. R. Dohner, A. R. Bowring, H. I. Karunadasa, M. D. McGehee, *Chem. Sci.* **2015**, *6*, 613.

[8] T. Leijtens, E. T. Hoke, G. Grancini, D. J. Slotcavage, G. E. Eperon, J. M. Ball, M. De Bastiani, A. R. Bowring, N. Martino, K. Wojciechowski, M. D. McGehee, H. J. Snaith, A. Petrozza, *Adv. Energy Mater.* **2015**, *5*, 1.

[9] C. Eames, J. M. Frost, P. R. F. Barnes, B. C. O'Regan, A. Walsh, M. S. Islam, *Nat. Commun.* **2015**, *6*, 7497.

[10] T. Y. Yang, G. Gregori, N. Pellet, M. Gratzel, J. Maier, *Angew. Chemie - Int. Ed.* **2015**, *54*, 7905.

[11] S. Van Reenen, M. Kemerink, H. J. Snaith, *J. Phys. Chem. Lett.* **2015**, *6*, 3808.

[12] S. Meloni, T. Moehl, W. Tress, M. Franckevičius, M. Saliba, Y. H. Lee, P. Gao, M. K. Nazeeruddin, S. M. Zakeeruddin, U. Rothlisberger, M. Graetzel, *Nat. Commun.* **2016**, *7*, 1.

[13] W. Tress, N. Marinova, T. Moehl, S. M. Zakeeruddin, N. Mohammad K., M. Grätzel, M. K. Nazeeruddin, M. Grätzel, *Energy Environ. Sci.* **2015**, *8*, 995.

[14] A. Walsh, D. O. Scanlon, S. Chen, X. G. Gong, S. H. Wei, *Angew. Chemie - Int. Ed.* **2015**, *54*, 1791.

[15] M. Cherry, M. S. Islam, C. R. A. Catlow, *J. Solid State Chem.* **1995**, *118*, 125.

[16] J. Mizusaki, K. Arai, K. Fueki, *Solid State Ionics* **1983**, *11*, 203.

[17] J.-P. Correa-Baena, A. Abate, M. Saliba, W. Tress, T. Jesper Jacobsson, M. Grätzel, A. Hagfeldt, *Energy Environ. Sci.* **2017**, *10*, 710.

[18] Y. Yuan, J. Chae, Y. Shao, Q. Wang, Z. Xiao, A. Centrone, J. Huang, *Adv. Energy Mater.* **2015**, *5*, 1.

[19] D. W. deQuilettes, W. Zhang, V. M. Burlakov, D. J. Graham, T. Leijtens, A. Osherov, V. Bulović, H. J. Snaith, D. S. Ginger, S. D. Stranks, *Nat. Commun.* **2016**, *7*, 1.

[20] C. Li, S. Tscheuschner, F. Paulus, P. E. Hopkinson, J. Kiessling, A. Koehler, Y. Vaynzof, S. Huettner, *Adv. Mater.* **2016**, *28*, 2446.

[21] A. Benninghoven, *Angew. Chemie - Int. Ed.* **1994**, 1023.

[22] T. Glaser, C. Mu, M. Sendner, C. Krekeler, O. E. Semonin, T. D. Hull, O. Ya, J. S. Owen, W. Kowalsky, A. Pucci, R. Lovrinc, *J. Phys. Chem. Lett* **2015**, 2913.
[23] N. Klein-Kedem, D. Cahen, G. Hodes, *Acc. Chem. Res.* **2016**, *49*, 347.
[24] Y. Luo, S. Gamliel, S. Nijem, S. Aharon, M. Holt, B. Stripe, V. Rose, M. I. Bertoni, L. Etgar, D. P. Fenning, *Chem. Mater.* **2016**, *28*, 6536.
[25] M. Stuckelberger, B. West, T. Nietzold, B. Lai, J. M. Maser, V. Rose, M. I. Bertoni, *J. Mater. Res.* **2017**, *32*, 1825.
[26] J. R. Poindexter, R. L. Z. Hoye, L. Nienhaus, R. C. Kurchin, A. E. Morishige, E. E. Looney, A. Osherov, B. Lai, V. Bulovic, V. Stevanovic, M. G. Bawendi, T. Buonassisi, *ACS Nano* **2017**, In press.
[27] R. P. Winarski, M. V. Holt, V. Rose, P. Fuesz, D. Carbaugh, C. Benson, D. Shu, D. Kline, G. Brian Stephenson, I. McNulty, J. Maser, G. B. Stephenson, I. McNulty, J. Maser, *J. Synchrotron Radiat.* **2012**, *19*, 1056.
[28] D. W. Dequilettes, S. M. Vorpahl, S. D. Stranks, H. Nagaoka, G. E. Eperon, M. E. Ziffer, H. J. Snaith, D. S. Ginger, *Sci.* **2015**, *348*, 683.
[29] S. Mastroianni, F. D. Heinz, J.-H. Im, W. Veurman, M. Padilla, M. C. Schubert, U. Würfel, M. Grätzel, N.-G. Park, A. Hinsch, *Nanoscale* **2015**, *7*, 19653.
[30] A. M. Soufiani, Z. Hameiri, S. Meyer, S. Lim, M. J. Y. Tayebjee, J. S. Yun, A. Ho-Baillie, G. J. Conibeer, L. Spiccia, M. A. Green, *Adv. Energy Mater.* **2016**, *7*, 1.
[31] A. M. Soufiani, M. J. Y. Tayebjee, S. Meyer, A. Ho-Baillie, J. Sung Yun, R. W. McQueen, L. Spiccia, M. A. Green, Z. Hameiri, *J. Appl. Phys.* **2016**, *120*, 1.
[32] U. Rau, *Phys. Rev. B - Condens. Matter Mater. Phys.* **2007**, *76*, 1.
[33] M. A. Green, *Prog. Photovolt Res. Appl.* **2012**, *20*, 472.
[34] P. Khoram, S. Brittman, W. I. Dzik, J. N. H. Reek, E. C. Garnett, *J. Phys. Chem. C* **2016**, *120*, 6475.
[35] J. Li, Q. Dong, N. Li, L. Wang, *Adv. Energy Mater.* **2017**, 1.
[36] K. Domanski, J. P. Correa-Baena, N. Mine, M. K. Nazeeruddin, A. Abate, M. Saliba, W. Tress, A. Hagfeldt, M. Gratzel, *ACS Nano* **2016**, *10*, 6306.
[37] K. Ando, A. Yamamoto, M. Yamaguchi, *J. Appl. Phys.* **1980**, *51*, 6432.
[38] I. E. Beckers, U. Fiedeler, S. Siebentritt, M. C. Lux-Steiner, *J. Phys. Chem. Solids* **2003**, *64*, 2031.
[39] N. N. Winogradoff, *Phys. Rev.* **1965**, *138*, A1562.
[40] H. Cho, S.-H. Jeong, M.-H. Park, Y.-H. Kim, C. Wolf, C.-L. Lee, J. H. Heo, A. Sadhanala, N. Myoung, S. Yoo, S. H. Im, R. H. Friend, T.-W. Lee, *Sci.* **2015**, *350*, 1222.
[41] J. Yan, B. Zhang, Y. Chen, A. Zhang, X. Ke, *ACS Appl. Mater. Interfaces* **2016**, *8*, 12756.
[42] J. Yan, X. Ke, Y. Chen, A. Zhang, B. Zhang, *Appl. Surf. Sci.* **2015**, *351*, 1191.
[43] K. Zheng, M. Abdellah, Q. Zhu, Q. Kong, G. Jennings, C. A. Kurtz, M. E. Messing, Y. Niu, D. J. Gosztola, M. J. Al-marri, X. Zhang, T. Pullerits, S. E. Canton, *J. Phys. Chem. Lett* **2016**, *7*, 4535.
[44] J. Haruyama, K. Sodeyama, L. Han, Y. Tateyama, *J. Am. Chem. Soc.* **2015**, *137*, 10048.
[45] J.-H. Yang, W.-J. Yin, J.-S. Park, S.-H. Wei, *J. Mater. Chem. A* **2016**, *4*, 13105.
[46] Z. Deng, B. Radhakrishnan, S. P. Ong, *Chem. Mater.* **2015**, *27*, 3749.
[47] H. Mashiyama, Y. Kawamura, H. Kasano, T. Asahi, Y. Noda, H. Kimura, *Ferroelectrics* **2007**, *348*, 182.
[48] T. J. Jacobsson, J. P. Correa-Baena, E. Halvani Anaraki, B. Philippe, S. D. Stranks, M. E. F. Bouduban, W. Tress, K. Schenk, J. Teuscher, J. E. Moser, H. Rensmo, A. Hagfeldt, *J. Am. Chem. Soc.* **2016**, *138*, 10331.

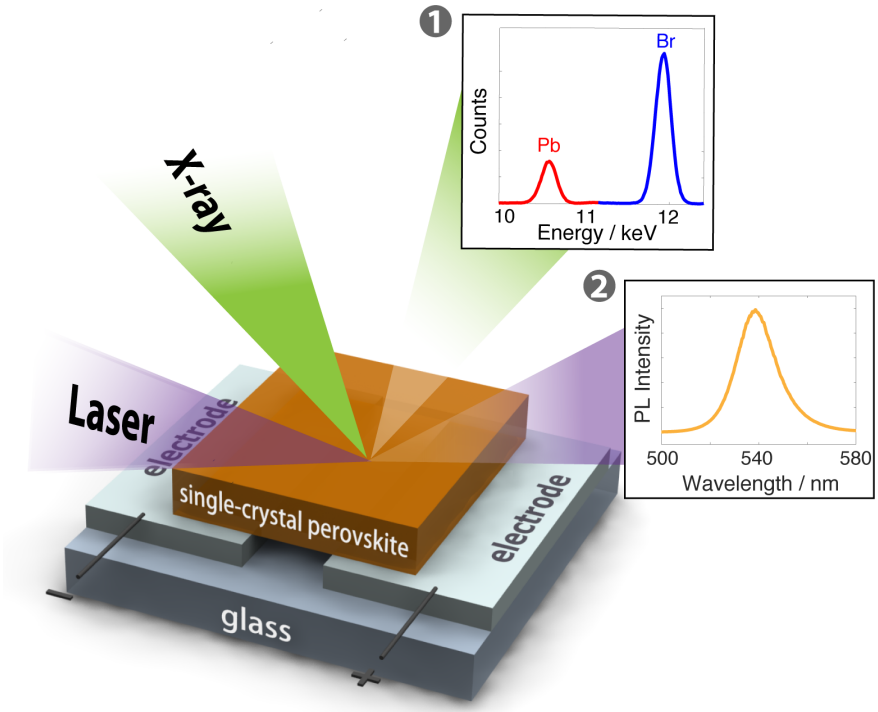

Figure 1. Photon-in Photon-Out Correlative Microscopy: schematic of nanoprobe X-ray fluorescence and spatially-resolved photoluminescence (PL) measurement. A 250 nm FWHM X-ray beam excites elemental fluorescence that reveals the local perovskite stoichiometry in single crystals bridging Pt-Pt electrodes. Subsequently, a laser beam excites optical luminescence to elucidate local optoelectronic quality. Note XRF and PL were not performed at the same time, but sequentially in a correlative microscopy approach.

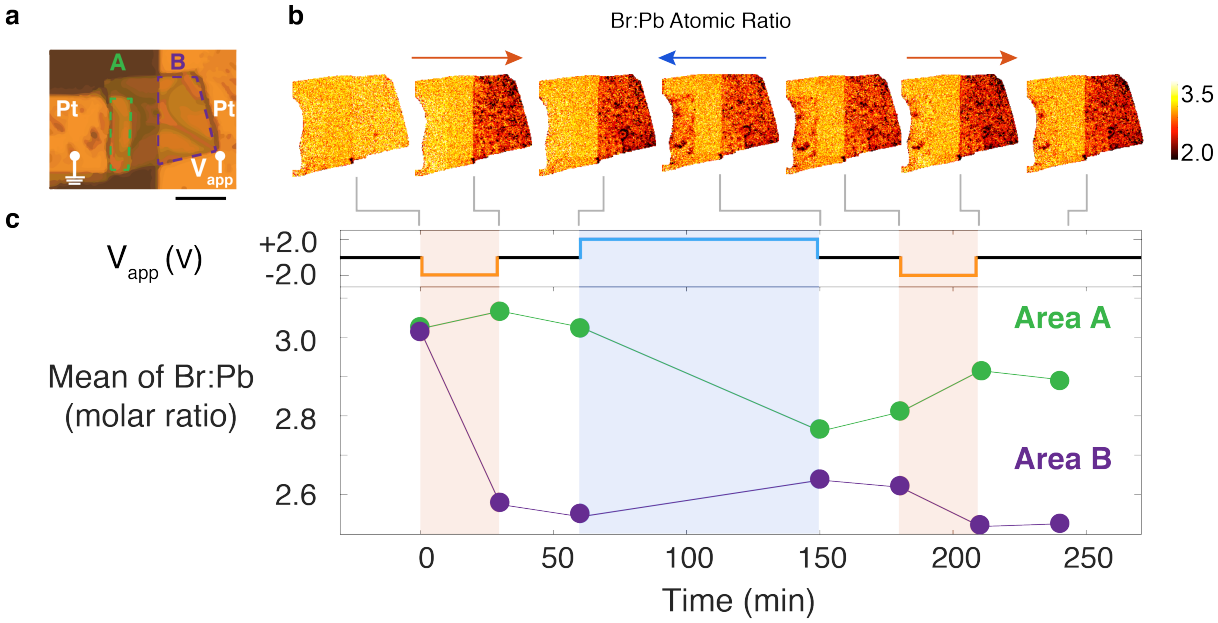

Figure 2. Nanoprobe X-ray fluorescence (Nano-XRF) measurement of the changes in elemental distribution in a $CH_3NH_3PbBr_3$ single crystal under bias. (a) An optical image of the $CH_3NH_3PbBr_3$ crystal characterized by nano-XRF. Regions A and B where the crystal covers the two different electrodes are indicated. The electrode under region A is grounded and the other electrode is biased. Scale bar is 15 µm. (b) X-ray fluorescence maps of the Br:Pb elemental ratio with 250 nm step size and 100 ms dwell time per point under a sequence of +/- 2V biases. The direction of the corresponding electric field for each map under bias is denoted by an arrow above the map (-2V orange and +2V blue). (c) The mean Br:Pb ratio of Area A and Area B (cf. Figure 2a) as measured by X-ray fluorescence during the bias sequence with the corresponding bias condition (top). Time spent at -2V is shaded in orange and +2V in blue.

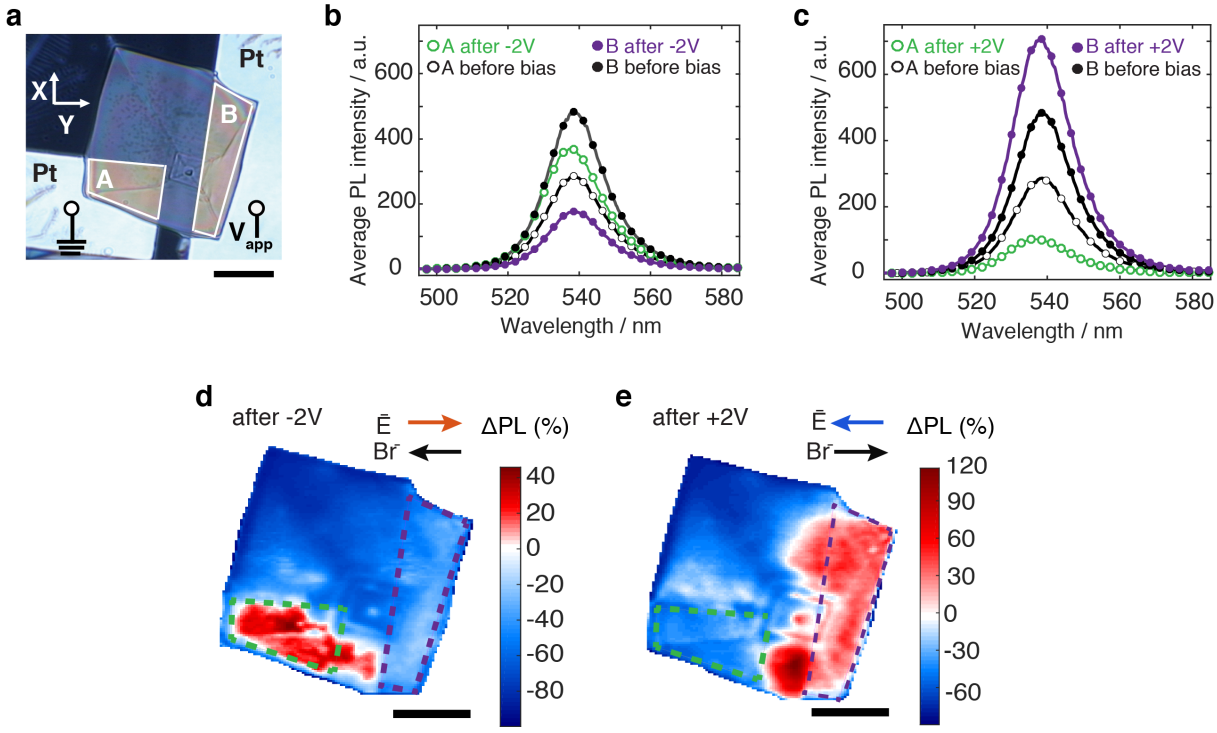

Figure 3. Photoluminescence variation of $CH_3NH_3PbBr_3$ after cyclic biasing. (a) Optical image of a hybrid perovskite crystal on Pt electrodes with labeled regions of interest A and B. (b) and(c) Overlaid photoluminescence spectra in Areas A and B after -2V and after +2V biasing, respectively. Black curves in each figure represent the initial PL intensity before any biasing in areas A and B. Plots with empty and filled markers correspond to average PL spectra of areas A and B, respectively. The corresponding spatially-resolved relative PL intensity maps are shown in (d) for -2V bias and (e) for 2V bias relative to the initial unbiased PL map. Scale bar is 10 µm.

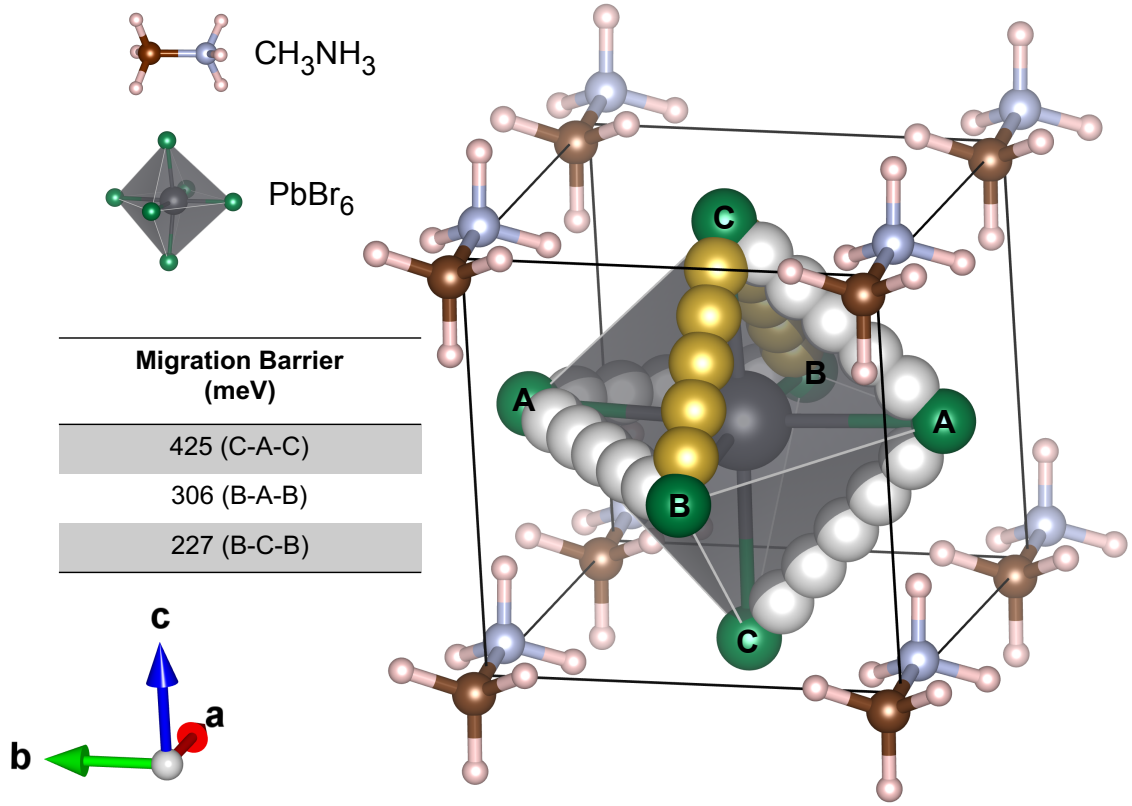

Figure 4. (a) Schematic of Br^- diffusion pathways in $CH_3NH_3PbBr_3$ by nudged elastic band (NEB). The $PbBr_6$ octahedron becomes distorted after NEB relaxation resulting in primitive cell has lattice constants of 6.017, 6.041, and 6.115 Å, along the *a-, b-,* and *c-axis*, respectively. The geometrically distinct Br atoms are labelled as A, B and C and the corresponding migration energy barriers between Br atoms are shown in the table. White spheres represent the interpolated Br trajectories along pathway B-A-B and C-A-C, while yellow spheres indicating the smallest barrier migration for pathway B-C-B.

Table of Contents (TOC):

Keywords: Hybrid perovskite; halide migration; nanoprobe x-ray fluorescence; spatially-resolved photoluminescence mapping; nudged elastic band (NEB) and DFT computation

Direct Observation of Halide Migration and its Effect on Photoluminescence of $CH_3NH_3PbBr_3$ Single Crystals

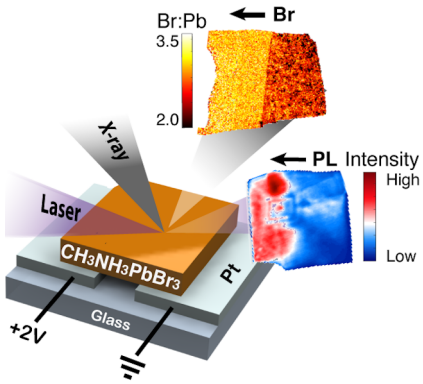

Supporting Information

Direct Observation of Halide Migration and its Effect on the Photoluminescence of $CH_3NH_3PbBr_3$ Single Crystals

Yanqi Luo,[1] Parisa Khoram,[2] Sarah Brittman,[2] Zhuoying Zhu,[1] Barry Lai[3], Shyue Ping Ong,[1] Erik Garnett,[2] David P. Fenning [1,]*

[1] Department of Nanoengineering, University of California San Diego,
La Jolla, CA 92093. dfenning@eng.ucsd.edu
[2] Center for Nanophotonics, AMOLF, Amsterdam, the Netherlands
[3] Advanced Photon Source, Argonne National Laboratory, Argonne, IL 60439

Materials and crystal fabrication

The organic precursor methylammonium bromide (MABr) was synthesized by adding hydrobromic acid (48 wt% in water, Sigma-Aldrich) into methylamine (33 wt% in ethanol, Sigma-Aldrich) dropwise in an ice bath and stirred for 2 h. The solvent was heated to 150 ˚C to allow solvents to evaporate, and the resulting powder was recrystallized from ethanol. The final organic precursor was dried by heating to 100-150 ˚C in air. $MAPbBr_3$ perovskite solution (1 M) was prepared by dissolving 1:1 mole ratio of MABr and $PbBr_2$ (Powder, 98%, Sigma-Aldrich) in dimethylformamide (DMF, anhydrous, 98%, Sigma-Aldrich). All solutions were prepared at room temperature in air. The deposition of the perovskite single crystals was followed by a previously published PDMS stamping technique.[1] The organic crystal has thickness of ~500 nm with a relatively smooth surface (15.4 ±3.9 nm rms roughness).

Synchrotron-Based XRF Characterization.

To determine the elemental distribution in the absorber, the perovskite crystals were investigated by synchrotron-based nanoprobe X-ray fluorescence (XRF) with a 250 nm full-width half-maximum focused beam at 13.6 keV with a 50% aluminum absorption filter in place at beamline 2-IDD in a helium environment of the Advanced Photon Source at Argonne National Laboratory. Fly-scanning was used with a dwell time per point of 100 ms. Using the beamline's nanopositioning stage, we scanned the sample in front of the focused X-ray beam and precisely mapped the local Pb and Br chemistry with a step size as small as 200 nm. An SRS 570 current

pre-amplifier at the beamline was used to bias the sample in-situ +/- 2V. **Figure 1** illustrates the experimental setup enabling the simultaneous collection X-ray fluorescence detection while applying a voltage bias across the crystal.

$MAPbBr_3$ stability was examined under focused X-ray beam at 13.6 keV with *no* filter in place (**Figure S2**). Br:Pb elemental ratio XRF maps indicate good stability of the material with no systematic change in its elements spatial distribution upon repetitive scanning with 100 ms dwell time per point.

In our analysis, we focus on the quantitative Br:Pb ratio. NIST standard reference material 1832 and 1833 standards were used to quantify the XRF data, correcting for the uncertainty in the extrapolation of the fluorescence yield to the Br line using the initial perovskite stoichiometry. Additional XRF maps of quantitative Pb:Pt and Br:Pt mass ratio are presented in **Figure S3**. Linear color scale is applied to each elemental ratio, where yellow indicates high mass ratio and red indicates low mass ratio.

Br:Pb center of mass analysis

To assess the movement of Br migration during bias and upon relaxation, the Br:Pb center of mass ($CoM_{Br:Pb}$) is calculated. First, the horizontal Br:Pb ($Br:Pb_{\_hor}$) distribution within the crystal is first obtained by taking the average of Br:Pb along each vertical line of pixels. Then the $CoM_{Br:Pb}$ is calculated using the **Eq. 1** using the corresponding distance *d*, where the left hand edge is $d = 0$ and right hand edge is $d = 30.4$ µm:

$$CoM_{Br:Pb} = \frac{\sum Br:Pb_{hor} \times d}{\sum Br:Pb_{hor}} \quad (1)$$

The $COM_{Br:Pb}$ is plotted respect to time and applied bias in **Figure S4.** Similar to **Figure 2** in the main text, the shaded colors indicate different bias conditions, where orange regions are -2V, white regions have no bias applied, and the blue region is +2V. Prior to any applied electric field, the $CoM_{Br:Pb}$ is almost in the middle of the crystal at ~15.20 µm. After the 1st bias applied, the $CoM_{Br:Pb}$ is shifted left toward the positive electrode nearly 0.8 µm due to the large depletion of Br observed on the right Pt electrode (Map 2, Figure 2a). Once the bias is removed (0V), the $CoM_{Br:Pb}$ relaxes back to the right to 14.48 µm, indicating Br^- back-diffusion upon relaxation of the applied potential. The relative magnitude of $CoM_{Br:Pb}$ shift under bias is in a range of 0.4-0.8 µm. In contrast, the shift of $CoM_{Br:Pb}$ is much smaller, from 0.07 to 0.2 µm, with no bias applied.

Subsequent cycling of the bias results in a repeatable shift of CoM in toward the positive electrode, and when the bias is removed, a motion opposite the previous migration toward the negative electrode.

Estimation of Br mobility

Given the applied voltage 2V and the gap space between electrodes 10 μm, the calculated E is 2000 V/cm. Our lower bound for the drift velocity v is estimated to be 5.56 x 10^{-7} cm/s using the distance d between electrodes and the 1800s duration t of apply bias, $v = d/t$. The lower bound estimate of the Br mobility at room temperature is calculated using Eq. 2, where v is the velocity, μ is the mobility and E is the applied electric field.

$$\mu = v/E \tag{2}$$

The resulting estimated mobility is 2.78 x 10^{-10} $cm^2/(V \cdot s)$.

Spatially resolved photoluminescence

A WITec alpha300 SR confocal imaging microscope was used to collect photoluminescence spectra of CH_3NH_3PbBr crystals while the crystal was being moved using a piezostage. Sample was excited with a 405 nm diode laser (Thorlabs S1FC405) through a NA 0.9 objective and the luminescence was collected in reflection using a UHTS 300 spectrometer. The spectral resolution of the spectrometer is < 0.09 nm. The calibration of the spectral response of the collection optics, fiber, and spectrometer was done with a standard mercury light source, and the spectrum was corrected accordingly.

The spatially-resolved PL maps are obtained by integrating the PL intensity within the optical fluorescence peak width, from 500-580 nm. The relative changes of PL intensity (ΔPL) is computed using equation 3,

$$\Delta PL^X\,(\%) = \frac{PLI^{\,X} - PLI_{\,initial\;0V}}{PLI_{\,initial\;0V}} \times 100 \tag{3}$$

where PLI is the photoluminescence intensity and X indicates the number of map according to Figure **S6**.

Additionally, the PL maps of $MAPbBr_3$ crystals on Au-Ti and Au-Au paired electrodes are shown in Figure **S7**. These maps display similar trends of PL intensity shifts under the influence of bias to the Pt-Pt electrodes shown in Figure 3.

Br vacancy migration barrier from NEB simulations

All density functional theory (DFT) calculations were performed using the Vienna *Ab initio* Simulation Package (VASP)[2] within the projector augmented-wave approach[3]. Spin-polarized calculations using the Perdew-Burke-Ernzerhof (PBE) generalized-gradient approximation (GGA)[4] functional were used for structure relaxations and all analyses were carried out using the Python Materials Genomics (pymatgen) library.[5]

We performed climbing image nudged elastic band (Cl-NEB) calculations using 2×2×2 supercells (8 formula units) of the lowest energy structure obtained for cubic $CH_3NH_3PbBr_3$ to minimize the interaction between periodic images. To study Br^- vacancy migration, a single positively-charge Br^- vacancy (V_{Br}^+) was introduced and overall charge neutrality was achieved by compensating background charge. A 2×2×2 *k*-point grid and energy cutoff of 520 eV were adopted for NEB calculations. The forces were converged to 0.05 eV/Å.

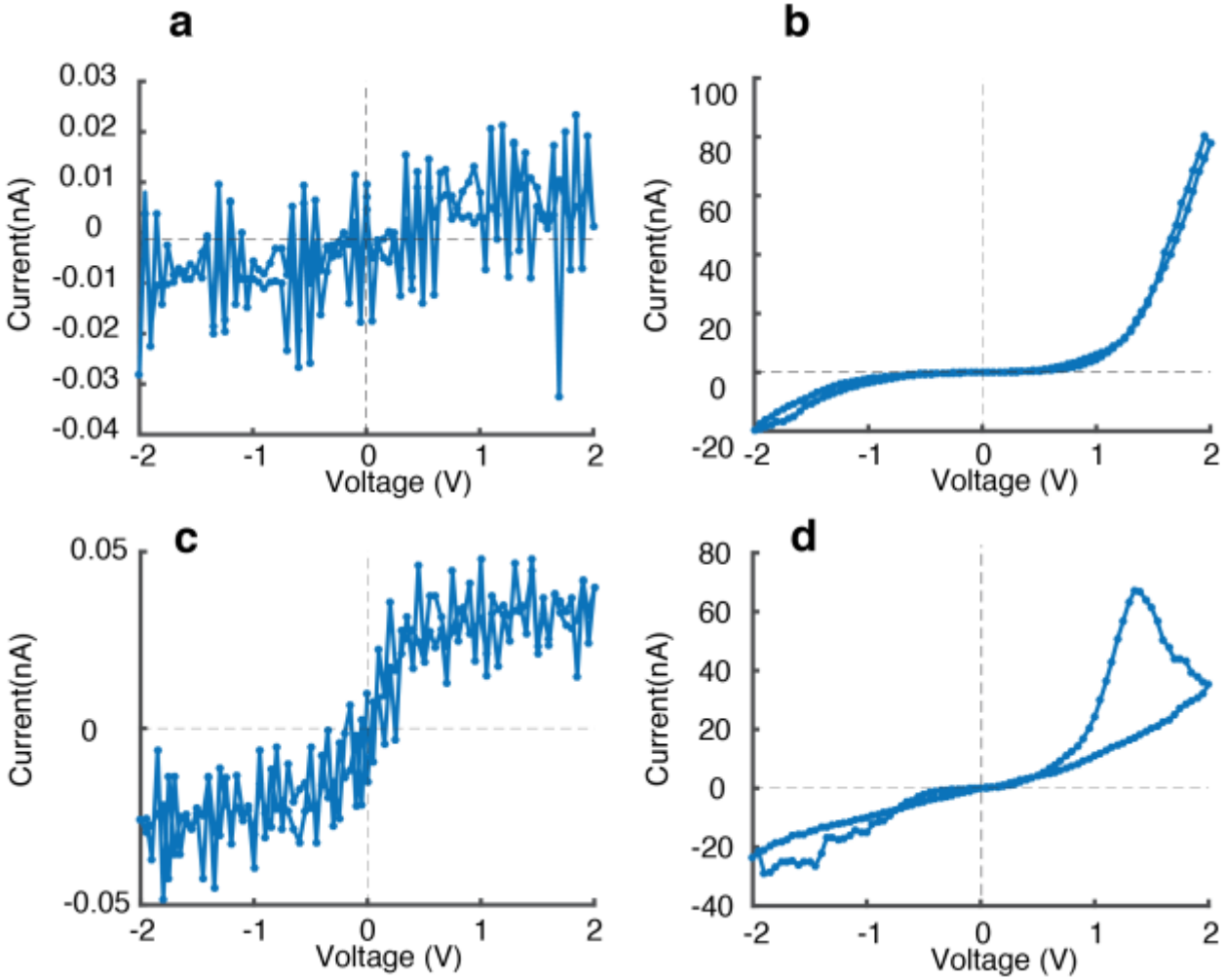

Figure S1. The electrical contact and photoresponse of $MAPbBr_3$ crystals on Pt-Pt electrodes were ensured before XRF and PL experiments. Current-voltage curves of $MAPbBr_3$ crystal before X-ray (for XRF) exposure under (a) dark condition, (b) AM1.5G illumination, crystal before laser (for PL) exposure under (c) dark condition and (b) AM1.5G illumination show clearly the crystals were electrically contacted to the electrodes and their current enhances by light illumination.

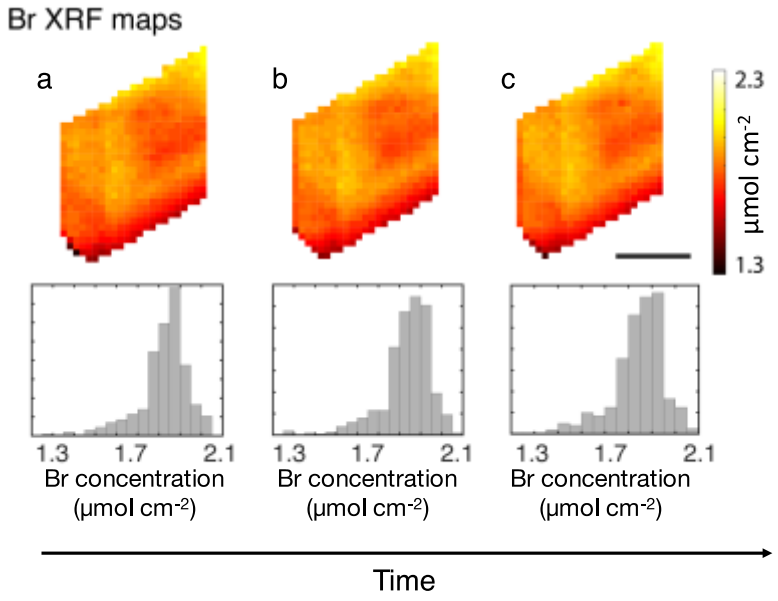

Figure S2. A $CH_3NH_3PbBr_3$ crystal under repetitive XRF measurement with full beam illumination. The Br XRF maps with the corresponding histograms are shown. The length of the scale bar is 5 µm. The mean and standard deviation for Map a, b and c are 1.82 ± 0.12, 1.83 ± 0.12, and 1.84 ± 0.11 µmol/cm^2, respectively.

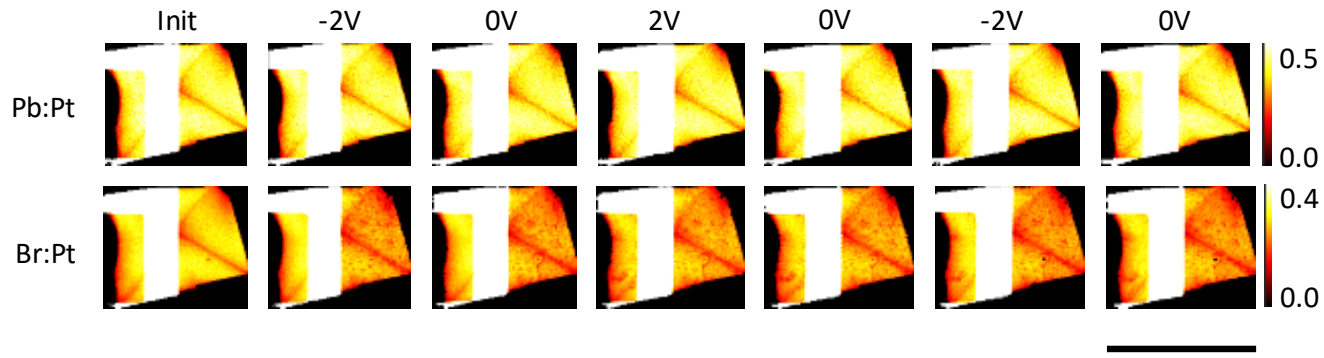

Figure S3. Pt:Pb and Pt:Br mass ratio XRF maps within the $MAPbBr_3$ crystal. The elemental ratio in each row has the same linear color scale. The scale bar is 33 µm.

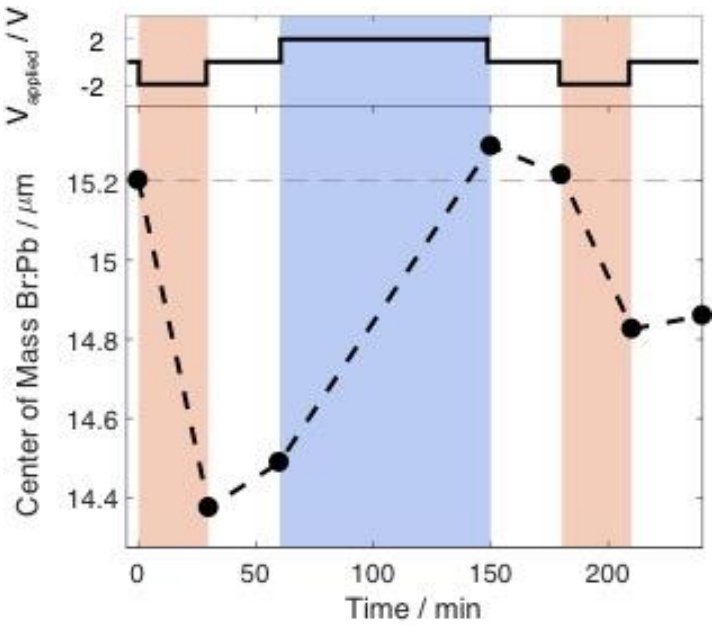

Figure S4. Br:Pb center of mass ($CoM_{Br:Pb}$) analysis on the elemental XRF maps over the entire perovskite crystal. The $CoM_{Br:Pb}$ shifts in the direction opposite the applied electric field, and relaxes back in reverse direction after the bias is removed.

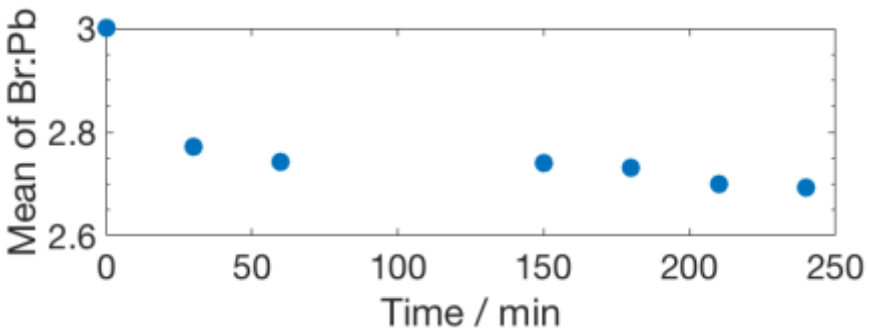

Figure S5. Average Br:Pb ratio with respect to time over the entire crystal as measured by nano-XRF in Figure 2.

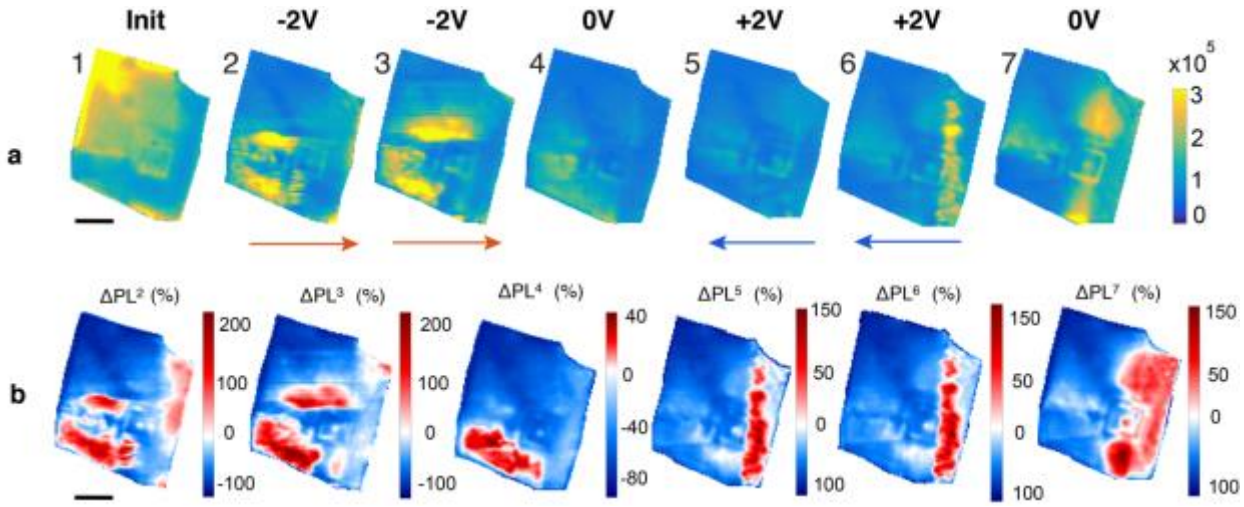

Figure S6. a) Spatially-resolved PL intensity maps. Each pixel of the maps is the integration of PL intensity at 500-580 nm. The bias condition is indicated above each map, and the direction of the electric field is indicated below with arrows if applicable. b) relative PL maps of the crystal in different bias conditions compared to the initial 0V map. ΔPL^4 and ΔPL^7 are shown in Figure 3d and e in the main text, respectively. The total time to collect each map was 30 min. Scale bar is 10 μm.

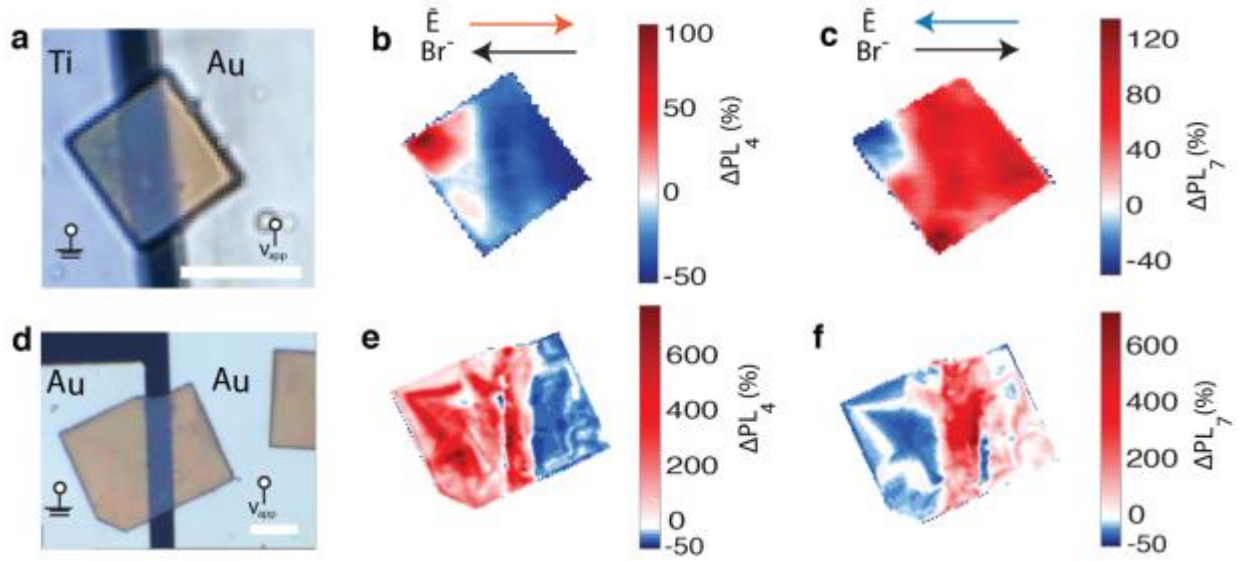

Figure S7. Series of relative PL maps for $CH_3NH_3PbBr_3$ crystal on Au-Ti (a-c) or Au-Au electrodes (d-f). The trend of an increase in PL intensity in the opposite direction of electric field is independent of electrode material. a) optical image of the crystal sitting on the gap between Au-Ti electrodes. b) relative PL intensity map of the crystal after applying -2V bias. c) relative PL intensity map of the crystal after applying +2V bias. d) optical image of the crystal sitting on the gap between Au-Ti electrodes. e) relative PL intensity map of the crystal after applying -2V bias. f) relative PL intensity map of the crystal after applying +2V bias. The arrows on top of each column show the direction of electric field and expected direction of Br^- movement. Scale bar is 10 μm.

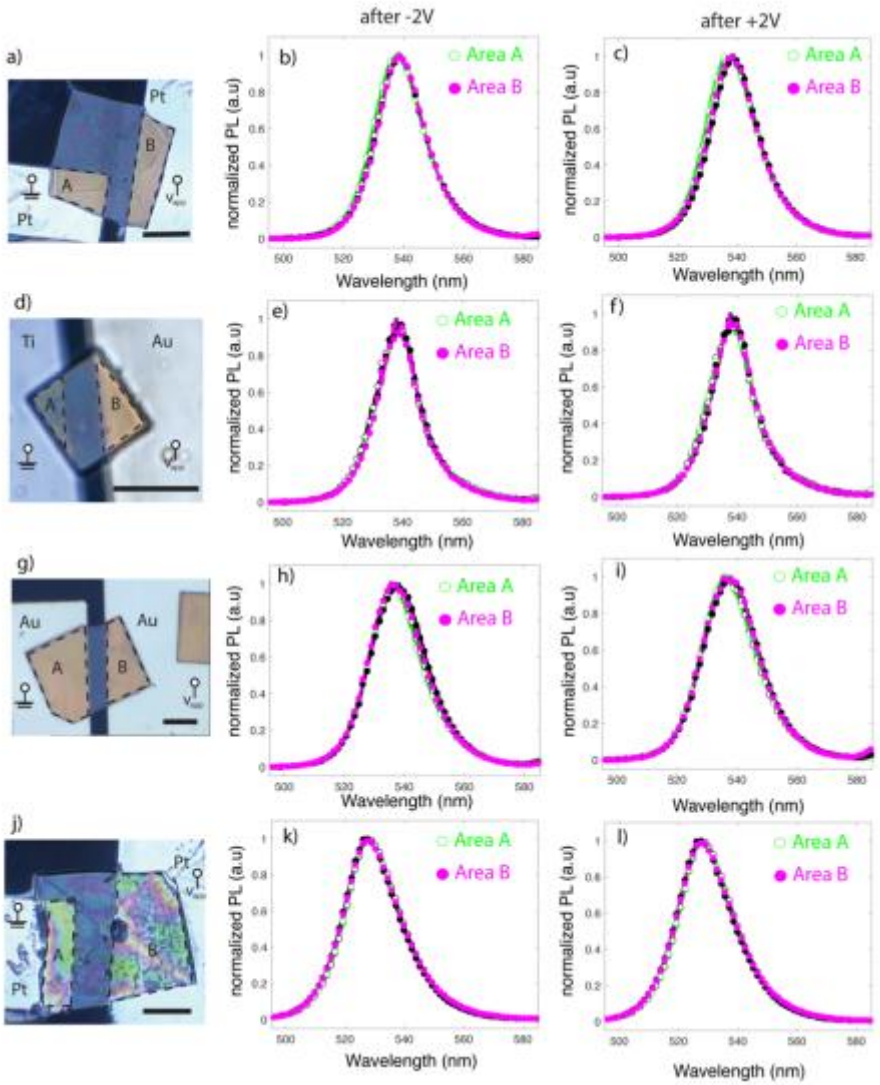

Figure S8. Normalized PL spectra of $CH_3NH_3PbBr_3$ crystals with different electrodes shows that the energy of PL peak does not vary upon applying electric field. The first column shows the optical image of the tested crystals on different electrode materials. Areas A and B are shown with dashed line on each figure. Second column presents normalized PL spectra after -2V poling for selected regions A and B. Third column shows normalized PL spectra after +2V poling for selected regions A and B. Scale bar is 10 μm.

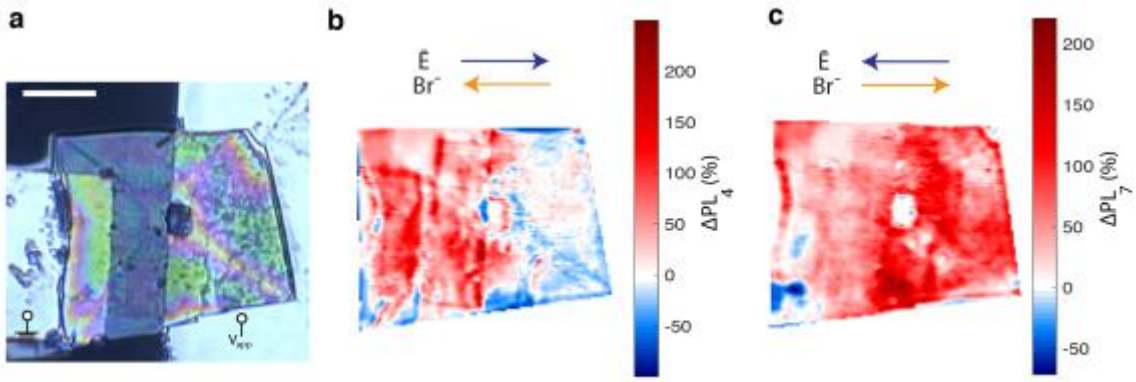

Figure S9. Percentage changes of PL intensity of the of $CH_3NH_3PbBr_3$ crystal after XRF measurement. (a) optical image of the crystal. (b) and (c) are relative PL maps after -2V and +2V poling respectively.

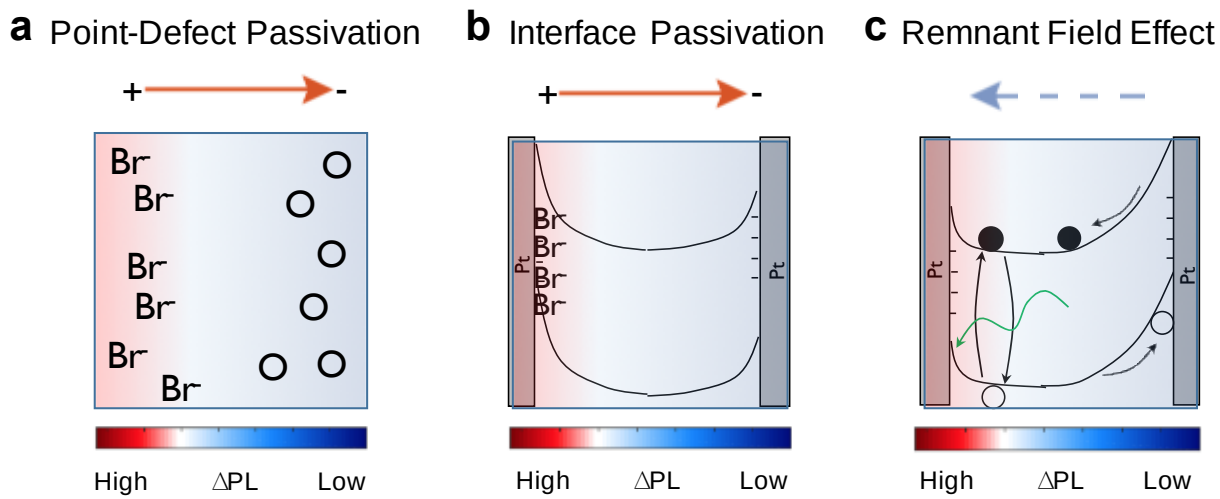

Figure S10. Schematic of mechanisms that can explain the observed PL intensity variation. At the positive (negative) electrode, Br migration may (a) reduce (increase) a vacancy-related, recombination active point-defect concentration, or (b) passivate (expose) surface states at the contact interface. Alternatively, (c) the remnant field due to slow ionic back-diffusion after the electric field is removed may leave a narrower (wider) depletion region.

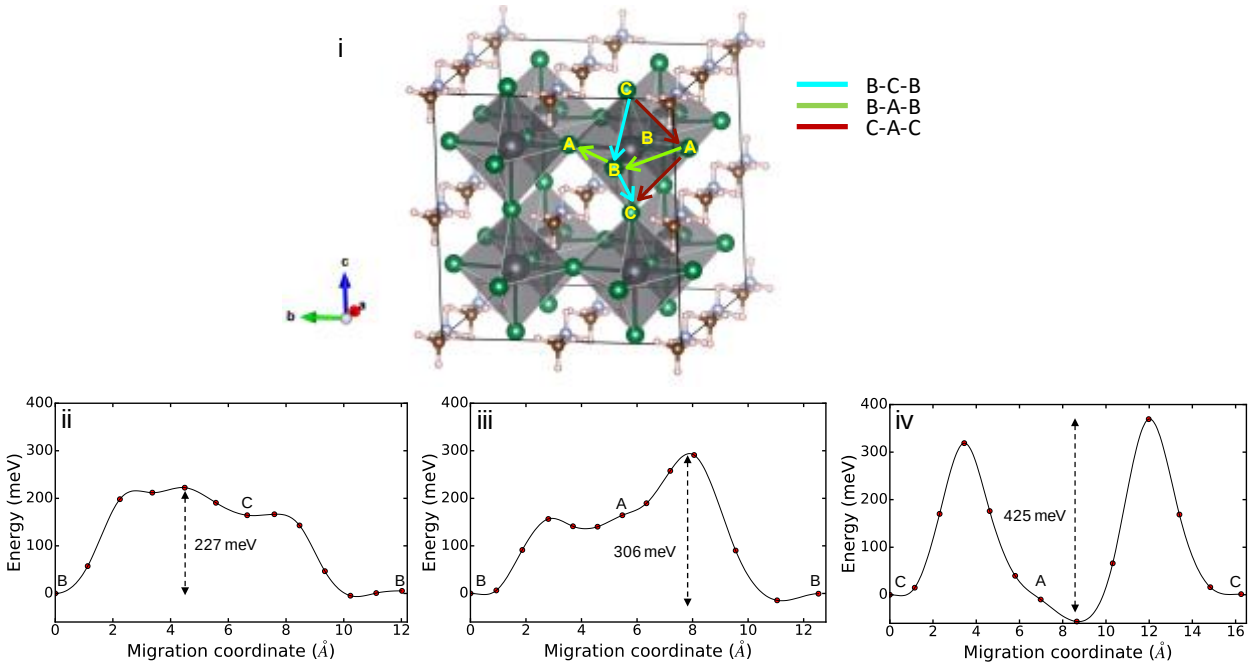

Figure S11. Br^- migration barriers from nudged elastic band (NEB) calculations. i) The migration paths depicted in the 2x2x2 super cell with paths labelled as B-A-B, B-C-B and C-A-C (labeled as in Figure 4). The energy vs migration coordinate of each path is shown: (ii) B-C-B, (iii) B-A-B, and (iv) C-A-C.

References:

[1] P. Khoram, S. Brittman, W. I. Dzik, J. N. H. Reek, E. C. Garnett, *J. Phys. Chem. C* **2016**, *120*, 6475.

[2] G. Kresse, J. Furthmüller, *Phys. Rev. B* **1996**, *54*, 11169.

[3] P. E. Blöchl, *Phys. Rev. B* **1994**, *50*, 17953.

[4] J. Perdew, K. Burke, M. Ernzerhof, *Phys. Rev. Lett.* **1996**, *77*, 3865.

[5] S. P. Ong, W. D. Richards, A. Jain, G. Hautier, M. Kocher, S. Cholia, D. Gunter, V. Chevrier, K. A. Persson, and G. Ceder, *Comput. Mater. Sci.* **2013**, *68*, 314.